Interfacial synthesis of mesoporous MnO_2/polyaniline hollow spheres and their application in electrochemical capacitors

Jian-Gan Wang [a,c], Ying Yang [b,d], Zheng-Hong Huang [a], Feiyu Kang [a,c,*]

[a] State Key Laboratory of New Ceramics and Fine Processing, Department of Materials Science and Engineering, Tsinghua University, Beijing 100084, China
[b] Department of Electrical Engineering, Tsinghua University, Beijing 100084, China
[c] Institute of Advanced Materials Research, Graduate School at Shenzhen, Tsinghua University, Shenzhen 518055, China
[d] State Key Laboratory of Control and Simulation of Power System and Generation Equipments, Tsinghua University, Beijing 100084, China

ARTICLE INFO

ABSTRACT

Mesoporous MnO_2/polyaniline composite (MP-I) has been synthesized using an interfacial synthesis technique. The results of X-ray diffraction and Fourier transform infrared spectroscopy indicate the amorphous structure of MP-I. The morphology of MP-I observed by scanning electron microscopy and transmission electron microscopy is composed of hierarchical hollow submicron spheres. The N_2 adsorption/desorption test reveals MP-I has higher surface area ($124 \, m^2 \, g^{-1}$) and more uniform pore-size distribution than the composite (MP-C) prepared by chemical co-precipitation. The electrochemical measurements show that as electrode materials the mesoporous MP-I composite electrode yields larger specific capacitance ($262 \, F \, g^{-1}$) with better rate capability and higher capacitance retention (93% of its initial capacitance after 800 cycles). The unique microstructure of MP-I and the coexistence of conducting polyaniline with MnO_2 are found to be responsible for the superior electrochemical properties.

© 2012 Elsevier B.V. All rights reserved.

1. Introduction

Electrochemical capacitors, also known as supercapacitors, are one of the most promising energy storage systems for power sources due to their high power density, fast charging/discharging rate and excellent long-term cyclability [1,2]. The most crucial factor determining the electrochemical performance consists in the electrode materials. Among the investigated electrode materials, transition metal oxides are considered to be good alternatives due to their high capacity from pseudocapacitance [3]. As a most competitive candidate, manganese oxides (MnO_2) have been received extensive research because of their intriguing characteristics such as ultrahigh theoretical specific capacitance (estimated to be $1370 \, F \, g^{-1}$), low cost, environmental friendliness and natural abundance [4,5]. However, the poor electrical conductivity (10^{-4}–$10^{-6} \, S \, cm^{-1}$) greatly reduces the utilization of bulk MnO_2 and thus only the surface or near surface (tens of nanometers in thickness) of MnO_2 is found to participate in the charge storage process [6,7].

One promising approach to resolve this problem is to incorporate nanostructured MnO_2 into conductive substrates, which provide high electroactive surface area and reliable electrical connection for a maximum utilization of MnO_2. Recently, considerable efforts in this respect have been devoted to explore conductive materials such as carbonaceous materials [8–15] and conducting polymers/inorganics [16–26]. The published results thus far demonstrated that this approach is of great effectiveness and significance. Among these studied substrates, conducting polymers are believed to be very useful because (i) the monomer can be soluble for in situ synthesis of MnO_2/conducting polymer composites and (ii) the polymer itself contributes to the pseudocapacitance. Up to now, MnO_2/poly(3,4-ethylenedioxythiophene) nanowires [16–19], MnO_2/polythiophene spheres [20], MnO_2/poly(3-methylthiophene) [21], MnO_2/polyaniline [22–25] and MnO_2/polypyrrole composites [26–28] have been developed as electrode materials. The combination of MnO_2 and conducting polymers would give rise to a strong synergic effect between each component [20,27], thus enhancing the electrochemical performance. However, the electrochemical performance is susceptible to the morphology of the MnO_2-based composites and the control of the morphology is rather challenging, which depends largely on the synthesis technique. Also, the porosity and pore-size distribution play important roles in determining the effective electroactive surface area that accessible to electrolyte ions and

the diffusion efficiency of electrolyte throughout the electrode. It is found that MnO_2 with ordered mesoporosity showed high specific capacitance with excellent rate capability [29]. Therefore, it would be of significance but a challenge to develop a synthesis technique to prepare mesoporous MnO_2-based composites.

In this work, we report a mesoporous MnO_2/polyaniline composite with unique hierarchical structure of hollow submicron spheres using a modified inorganic/organic interfacial synthesis technique [20,30]. This is a simple one-step process without using any sacrificed templates or surfactants. The physical characteristics and electrochemical properties of the resulted products are investigated thoroughly via X-ray diffraction, Fourier transform infrared spectroscopy, scanning electron microscopy transmission electron microscopy and N_2 adsorption/desorption test as well as electrochemical measurements. The formation mechanism and the effect of microstructure on the electrochemical capacitive behaviors of the binary composites are also discussed.

2. Experimental

2.1. Preparation of MnO_2/polyaniline composites

All chemicals were of analytical grade and used as-purchased. In the interfacial synthesis, aniline monomers (5 mmol) were dissolved in 50 ml organic Trichloromethane ($CHCl_3$) solution. Potassium permanganate ($KMnO_4$, 5 mmol) was dissolved in 50 ml distill water and several drops of hydrochloride acid were added to the aqueous $KMnO_4$ solution to adjust the pH value to 1. Both solutions were pre-cooled to 0–5 °C and then the aqueous solution was added slowly into the organic solution. An obvious interface was formed immediately between the organic phase and aqueous phase. The reaction vial was kept statically in a refrigerator with a controlled temperature of 0–5 °C for 6 h. During the reaction, the aniline was diffused from the organic solution to the interface and was chemical oxidized into polyaniline. At the same time, MnO_4^- was reduced to manganese oxide precipitates. Finally, the products remained in the aqueous solution. For comparison, conventional chemical co-precipitation of MnO_2/polyaniline composite was performed as following. Aniline monomers (0.1 M) and $KMnO_4$ (0.1 M) were dissolved into 0.1 M HCl solution and distill water, respectively. Then the pre-cooled $KMnO_4$ solution was poured into the aniline solution and stirred for 15 min to obtain a homogenous mixture. Then the mixture was placed alone in a refrigerator at 0–5 °C for 6 h. Both precipitates were filtered and washed with ethanol and distill water thoroughly to remove the residuals. The resulting products were dried at 60 °C for 12 h. The MnO_2/PANi composites prepared by interfacial synthesis and chemical co-precipitation were denoted as MP-I and MP-C, respectively.

2.2. Materials characterization and electrochemical evaluation

X-ray powder diffraction (XRD, Rigaku D/Max 2500PC, Japan) was employed to study the crystal structures of the composites. The Fourier transform infrared (FTIR) spectra were recorded on Nicolet 6700 with the sweeping range of 400–4000 cm^{-1} at a 4 cm^{-1} resolution with KBr as compressed slices. The morphology of the products was investigated with a field emission scanning electron microscopy (FESEM, LEO-1530) and a high-resolution transmission electron microscopy (HRTEM, JEOL 2010). Thermogravimetric analysis (TGA) was performed on a TA instrument SDT-Q600 with temperature increments of 10 °C min^{-1} in N_2 atmosphere. The textual characteristics were investigated using N_2 physical adsorption–desorption test at a liquid nitrogen temperature of −196 °C on a Belsorp Max apparatus (Japan). The specific surface area (S_{BET}) was determined by Brunauer–Emmett–Teller (BET)
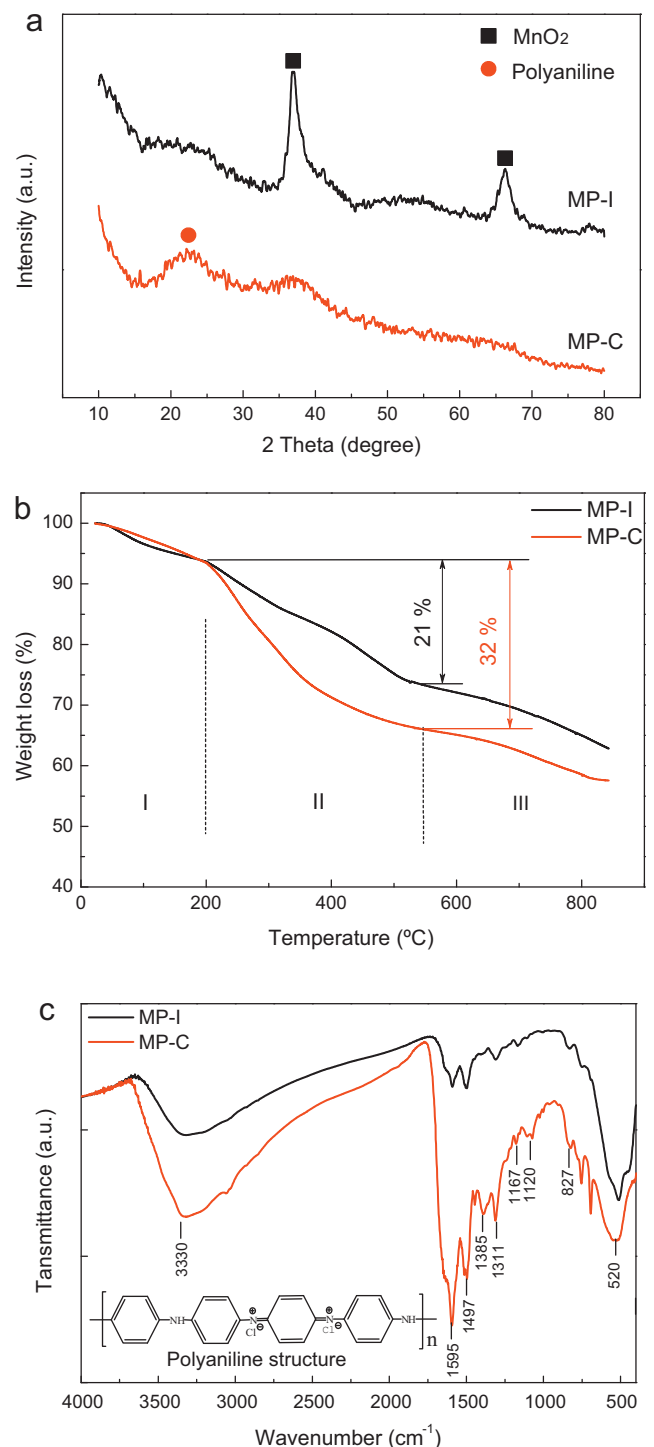

Fig. 1. (a) XRD patterns; (b) TGA profiles and (c) FTIR spectra of MnO_2/polyaniline composites.

method. The pore size distribution was calculated according to the Berrett–Joyner–Halenda (BJH) method.

The electrodes for evaluating the electrochemical performance of as-prepared MnO_2/PANi composites were fabricated by mixing the composites with carbon black (20 wt.%) and polytetrafluoroethylene binder (PTFE, 10 wt.%). A slurry of the above mixture was made using ethanol as a solvent which was subsequently brush-coating onto Ni foam with an effective area of ∼1 cm^2. The foam was dried at 60 °C in air for 30 min in order to remove the solvent, and then uniaxially pressed under 10 MPa. The mass

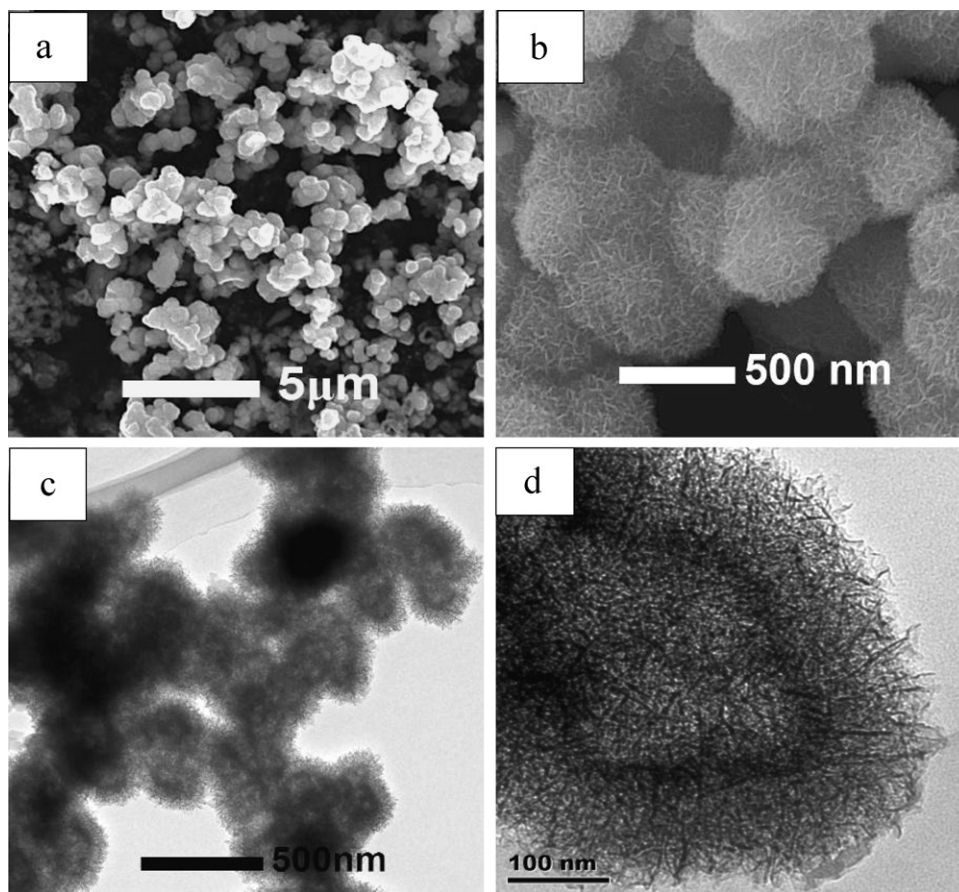**Fig. 2.** SEM (a and b) and TEM (c and d) images of MP-I composites.

loading of the active materials is $3.0 \, \text{mg cm}^{-2}$. Electrochemical measurements were carried out on the CHI 660B electrochemical station in a three-electrode configuration with the Ni foam as the working electrode, platinum wire and saturated calomel electrode (SCE) as counter and reference electrode, respectively. The cyclic voltammetry and galvanostatic charging/discharging techniques were employed to study electrochemical performance of the electrodes with a potential window ranging from -0.1 to $0.8 \, \text{V}$ in a $0.5 \, \text{M Na}_2\text{SO}_4$ electrolyte. The electrochemical impedance spectroscopy was conducted in the frequency range between $100 \, \text{kHz}$ and $20 \, \text{mHz}$ with perturbation amplitude of $5 \, \text{mV}$ versus the open-circuit potential. The average specific capacitance values are calculated from the CVs and discharging curve according to Eqs. (1) and (2), respectively:

$$C = \frac{1}{m \cdot v \cdot \Delta V} \int i(V) dV \tag{1}$$

$$C = \frac{I \cdot \Delta t}{m \cdot \Delta V} \tag{2}$$

where m is the mass of active materials, v is the potential scan rate, ΔV is the potential window, $i(V)$ is the voltammetric current, I is the applied current and Δt is the discharging time.

3. Results and discussion

3.1. Structural characterization

Fig. 1(a) shows the XRD patterns of the as-prepared MnO_2/polyaniline composites. For MP-I composite, the characteristic peaks around $2\theta = 37°$ and $66°$ can be readily indexed to the

hexagonal birnessite-type MnO_2 with cell parameters of $a = b = 5.82 \, \text{Å}$, $c = 12.62 \, \text{Å}$ (JCPDS 18-0802). The broadness of the peaks reveals the amorphous nature of MP-I composite. Birnessite-type MnO_2 has a 2D lamellar structure with an interlayer distance about $7 \, \text{Å}$, which is suitable for insertion/extraction of alkali cations in the electrochemical storage process [20]. There is no obvious peak for polyaniline, indicating MnO_2 is predominant in MP-I. By contrast, two weak peaks at $2\theta = 22°$ and $37°$ are observed on MP-C composite, which can be assigned to polyaniline [31] and MnO_2, respectively. The relative low-intensity and broad profiles suggest the low degree of crystallinity of both components. The stronger intensity of MnO_2 peaks for MP-I also indicates the greater content of MnO_2 than that in MP-C, as also confirmed by TG analysis. Three major weight losses are observed in the TGA profiles of the as-prepared materials, as shown in Fig. 1(b). The first weight loss below $200 °\text{C}$ is attributed to the physically adsorbed water on the surface of the samples. The second weight loss in the temperature range of 200–$540 °\text{C}$ corresponds to the removal of doping anions from the polymer structure and degradation of the polyaniline chain [32]. The weight percent of polyaniline is about $21 \, \text{wt.\%}$ and $32 \, \text{wt.\%}$ for the MP-I and MP-C, respectively. The last stage above $540 °\text{C}$ is related to the evolution of oxygen and chemically water molecules from MnO_2.

The structure and component of the prepared MnO_2/polyaniline composites are further elucidated by Fourier transform infrared spectroscopy, as shown in Fig. 1(c). The adsorption peaks reveal the presence of both polyaniline and MnO_2, and can be identified as follows [22,31,33,34]. The characteristic peaks at $1595 \, \text{cm}^{-1}$ and $1497 \, \text{cm}^{-1}$ can be assigned to the stretching vibration of quinoid ring and benzenoid ring, respectively. The peaks at $1120 \, \text{cm}^{-1}$ and
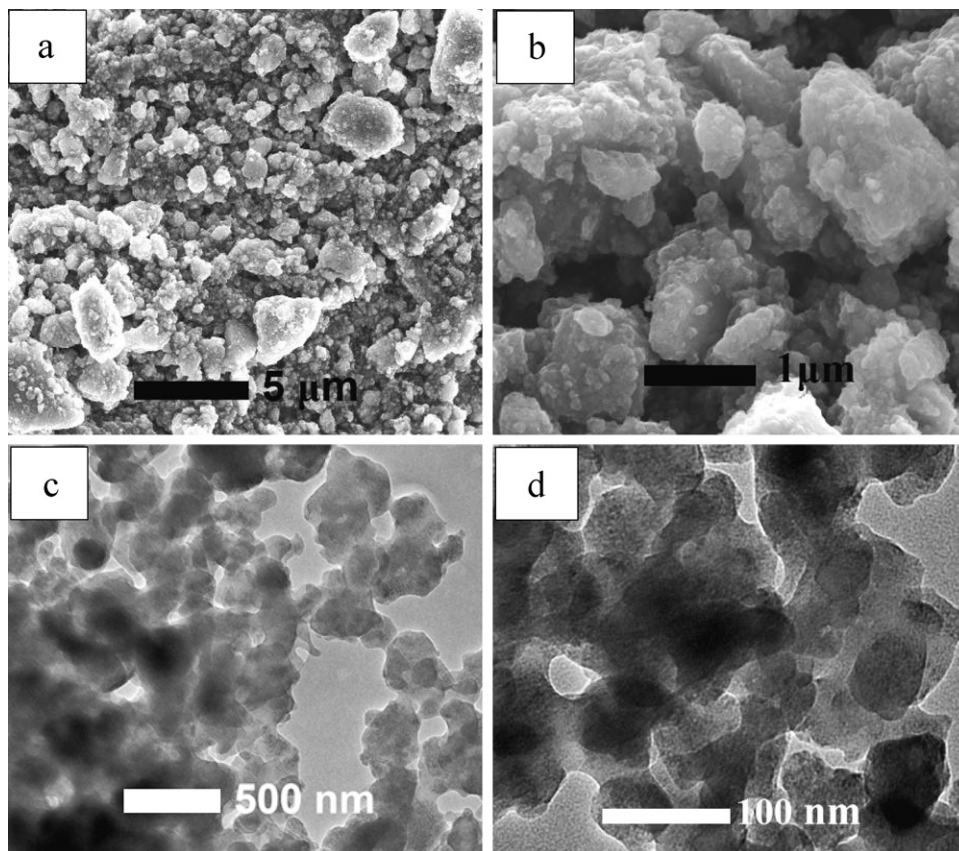
Fig. 3. SEM (a and b) and TEM (c and d) images of MP-C composites.

$827\,cm^{-1}$ are attributed to the in-plane vibration and the out-of-plane deformation of C—H in benzene ring, respectively. The peak at $1311\,cm^{-1}$ belongs to the Ph—N stretching vibration of an aromatic amine. These characteristic peaks are consistent with the emeraldine salt structures of polyaniline [34], as drawn in the inset of Fig. 1(b). In addition, the peaks appeared at $1385\,cm^{-1}$ and $1167\,cm^{-1}$ are related to the polyaniline conductivity and a degree of delocalization of electrons, indicating the polyaniline is to an extent doped by HCl [35]. The bands at $3300\text{–}3500\,cm^{-1}$ can be assigned to stretching vibrations of physical adsorbed water molecules. The wide band in the regions from 500 to $800\,cm^{-1}$ can be assigned to Mn—O stretching vibrations.

3.2. Morphology observation and formation mechanism

The FESEM images of the as-prepared composites are shown in Fig. 2. The morphology of MP-I products in Fig. 2(a) indicates that the composite is composed of agglomerated submicron spheres with diameters ranging from 300 nm to 600 nm. The agglomeration is due to the high surface energy of the spheres. The high-magnification FESEM feature showed in Fig. 2(b) clearly illustrates the nanostructured petal-shape nanosheets on the surface of the spheres. The hierarchical microstructure can be further confirmed by the TEM imaging, as present in Fig. 2(c and d). Interestingly, it is observed from Fig. 2(d) that the as-prepared MP-I submicron spheres have a unique hollow structure with a shell thickness about 150 nm. For comparison, the contrasting morphology of the MP-C composite prepared by chemical co-precipitation route is shown in Fig. 3. Obviously, the MP-C composite is composed of densely agglomerated particles having a rough diameter about 50 nm.

The different morphology can be rationalized by the formation mechanism, as schematically illustrated in Fig. 4. For the interfacial synthesis, the redox reaction occurs at the aqueous/organic interfacial region, where the polymerization of aniline monomers are chemical oxidized by MnO_4^- ions concurrent with the formation of MnO_2 products by reducing MnO_4^-. This coupling reaction proceeds through a slow diffusion of aniline into the reactive interface, as shown in Fig. 4(a). The slow process favors the self-assembly growth of hollow MnO_2/polyaniline submicron spheres. Afterwards, the hydrophilic nature of the MnO_2/polyaniline composite would drive the composite diffuse away from the interface into the upper aqueous phase [36], thus preventing the contact between MnO_2 and aniline monomers. A recent literature reported an interfacial synthesis of MnO_2/polyaniline composites [30], in which the irregular morphology of their products is totally different from the present one. The reason may be attributed to the difference in pH value of the aqueous solution. In our study, the aqueous solution was adjust to pH = 1 by hydrochloric acid (compared to pH = 7 in the literature), since hydrochloric acid can be used as dopant to improve the electrical conductivity of polyaniline. The comparison reveals the importance of delicate control of the synthesis conditions to engineering the composite's morphology. In the chemical co-precipitation, due to the reaction occurs throughout a single aqueous phase, a great number of MnO_2/polyaniline nuclei are formed, which would grow to a small final size in agglomerated morphology (Fig. 4(b)). Note that the oxidation potential of MnO_2 (1.23 V) is even higher than that of aniline (0.5 V) [37], the highly active MnO_2 nanoparticles would also act as oxidants to polymerize the aniline monomers. The MnO_2 precipitates formed in chemical co-precipitation, not like those in interfacial synthesis, are directly exposed to the aniline monomers during the whole
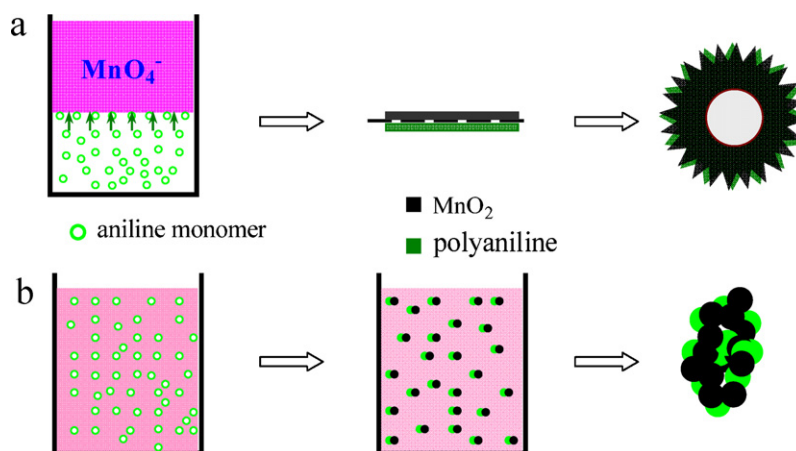
Fig. 4. Schematic illustration of the formation mechanisms of MnO_2/polyaniline composites: (a) interfacial synthesis and (b) chemical co-precipitation.

process. This would result in partial reduction of MnO_2 by aniline, which accounts for the fact that the content of MnO_2 in MP-C composite is lower than that in MP-I composite.

3.3. Textural characterization of MnO_2/polyaniline composites

N_2 adsorption/desorption tests are performed to characterize the specific surface area and the pore-size distribution of both samples, and the resulting isotherms and BJH plots are given in Fig. 5. The isotherm of MP-I composite in Fig. 5(a) shows a typical IUPAC type IV isotherm with a hysteresis loop of type H3, suggesting its typical mesoporous structure. The calculated BJH pore-size distribution is narrow and centers around 4 nm, as depicted in the inset of Fig. 5(a). Such a well-defined mesoporous structure arises from the hierarchical self-assembly of ultrathin nanosheets giving rise to slit-shaped pores [38], which may be beneficial for the electrolyte ion transport. By contrast, the isotherm of MP-C composite
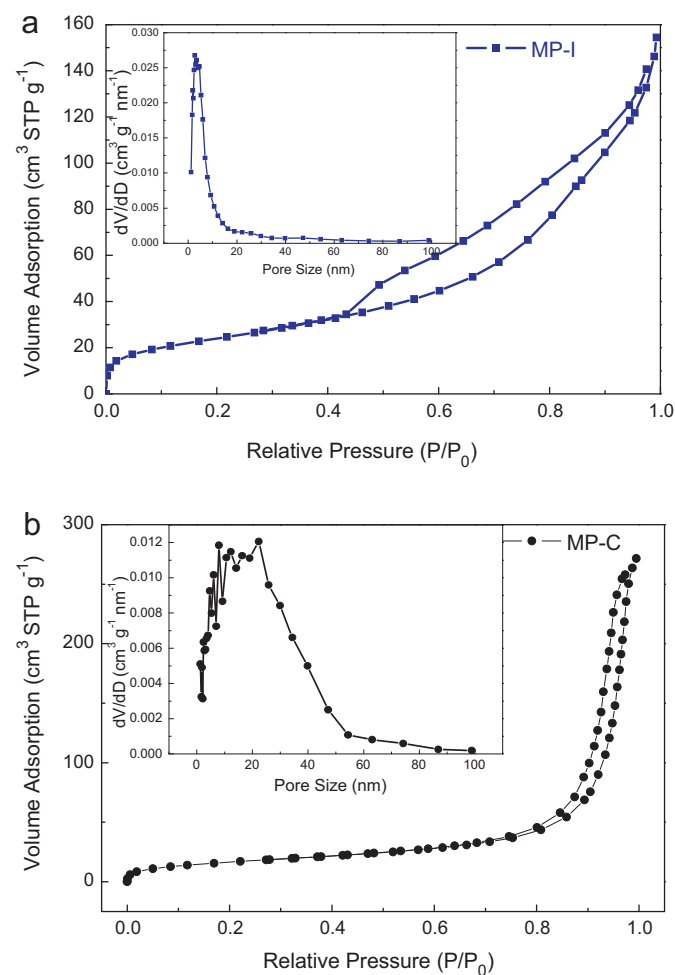

Fig. 5. N_2 adsorption–desorption isotherms and the corresponding pore-size distribution of (a) MP-I and (b) MP-C composites.
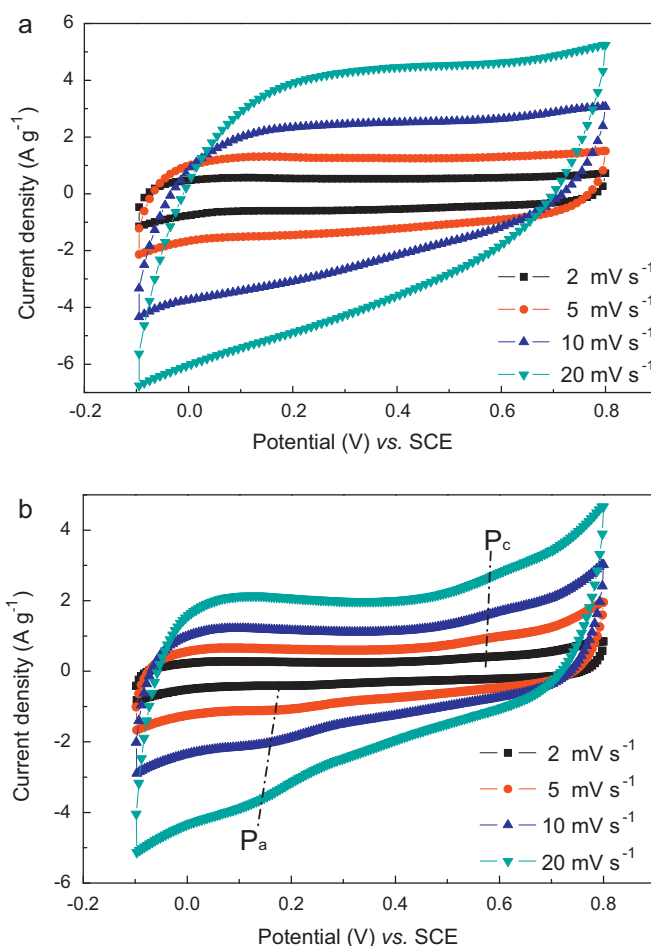

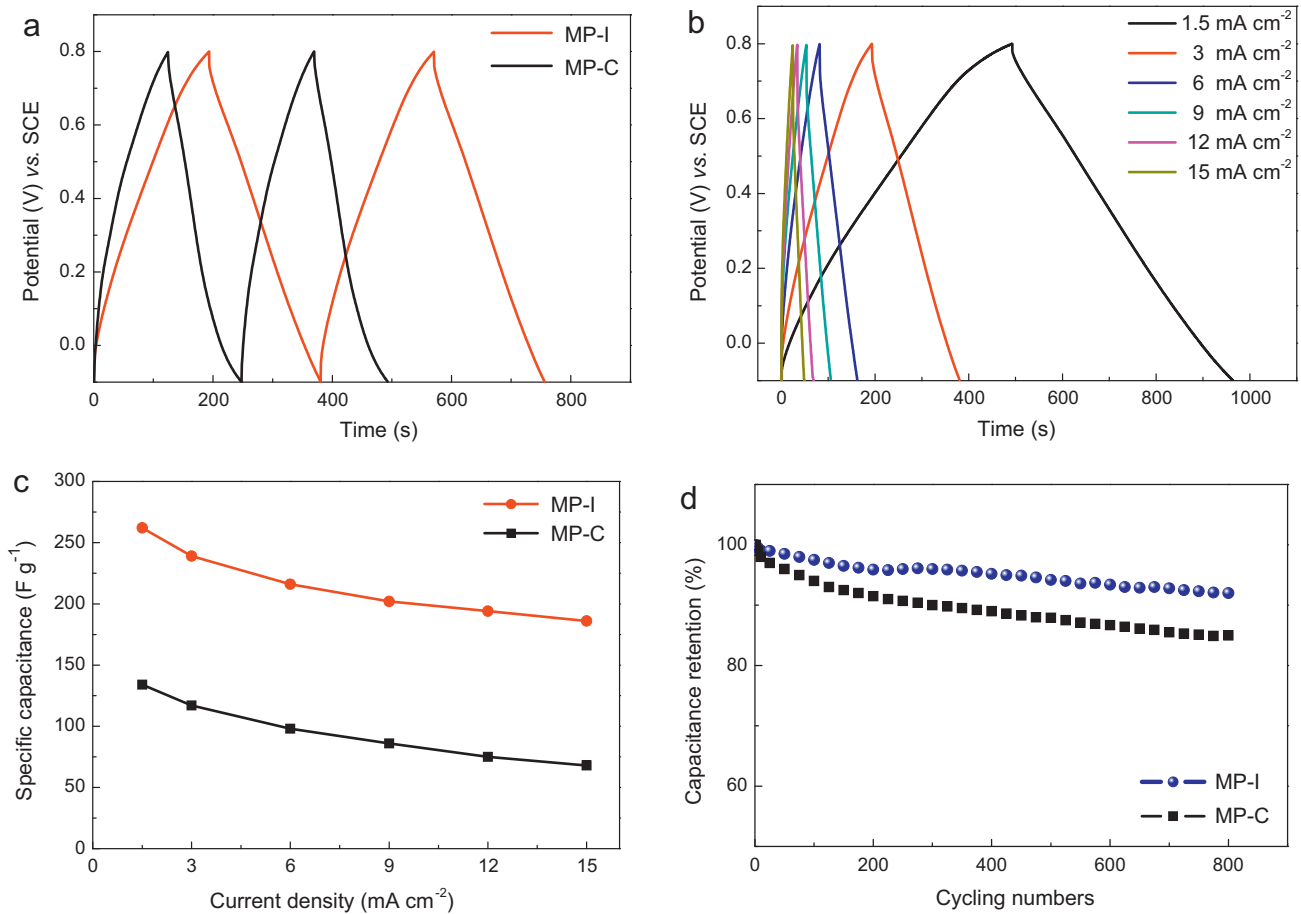**Fig. 6.** Cyclic voltammograms of the composites electrodes at different scan rates: (a) MP-I and (b) MP-C composite.

Fig. 7. (a) Galvanostatic charging/discharging curves of both composites at 3 mA cm^{-1}. (b) Galvanostatic charging/discharging curves of MP-I composite at various current densities. (c) Dependence of specific capacitance on the current density. (d) Capacitance retention as a function of cycling numbers at 9 mA cm^{-1}.

is of IUPAC type II, displaying a small hysteresis loop in the relative pressure range above 0.8. This isotherm indicates the random pores with a broad pore-size distribution, as shown in Fig. 5(b). The BET specific surface area of MP-I and MP-C composites are quantified to be 124 m^2 g^{-1} and 61 m^2 g^{-1}, respectively. Hence, mesoporous MP-I composite is expected to provide more accessible electroactive sites for electrolyte ions during charging/discharging process.

3.4. Electrochemical performance

The electrochemical properties of the as-prepared MnO$_2$/polyaniline composites are evaluated using typical cyclic voltammetry (CV) and galvanostatic constant current charging/discharging technique. Fig. 6 shows the CV curves of MP-I and MP-C composites at various scan rates. As seen from Fig. 6, the CV curves of both composites exhibit near rectangular and enantiomorphous profiles, indicating ideal pseudocapacitive behaviors and highly reversibility. It is worthy to note that the MP-I composite electrode exhibits much larger current density than MP-C composite one at the same scan rate, demonstrating the former have much higher specific capacitance. The specific capacitance values of MP-I composite calculated from Eq. (1) are 253, 231, 212, 196 F g^{-1} at the scan rates of 2, 5, 10 and 20 mV s^{-1}, respectively, which are almost twice amount of MP-C composites at each scan rate. The higher specific capacitance of MP-I composite can be explained by its greater electroactive surface area accessible to electrolyte. Additionally, a couple of weak redox peaks (P_c/P_a) can be observed on the CVs of MP-C composites, which stems from the redox transition of polyaniline between a

semiconducting state (leucoemeraldine form) and a conducting state (polaronic emeraldine form) [34]. This suggests conducting polyaniline component makes partial contribution to the overall capacitance of the composites. The redox peaks are not obvious in MP-I composite because of its low content of polyaniline.

Fig. 7(a) displays the representative galvanostatic charging–discharging curves of MnO$_2$/polyaniline composites at a current density of 3 mA cm^{-2}. The good symmetric profiles and linear slopes with respect to charging and discharging indicate good capacitive behavior for both composites. The charging–discharging curves of MP-I composite at different current densities (1.5–15 mA cm^{-2}) are illustrated in Fig. 7(b) and the resulting dependence of the specific capacitance (Eq. (2)) for both composites on current density is plotted in Fig. 7(c). It can be seen that both capacitances decrease with the increase in the applied current density. Two storage mechanisms have been proposed for MnO$_2$ materials [2]. The first one is based on the surface adsorption/desorption of protons or alkali cations from electrolyte, as expressed in Eq. (3). The capacitance depends on the surface area of MnO$_2$, which is usually predominant in amorphous MnO$_2$. The second mechanism involves the insertion/extraction of protons or alkali cations into the tunnel structure of crystalline MnO$_2$ with a concomitant redox between Mn^{3+} and Mn^{4+}, as expressed by Eq. (4). This process is related to the tunnel size, which should be large enough (such as α-MnO$_2$) to accommodate the cations.
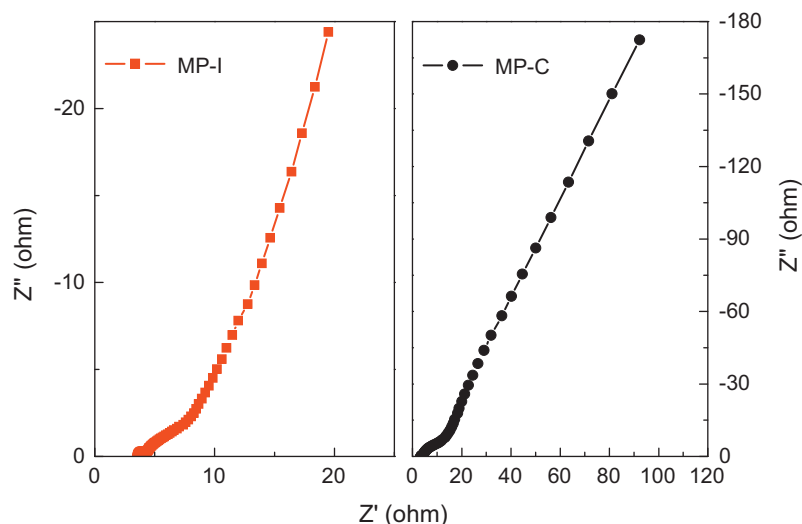
$$(MnO_2)_s + M^+ + e \leftrightarrow (MnOOM)_s \tag{3}$$

$$MnO_2 + M^+ + e \leftrightarrow MnOOM \tag{4}$$
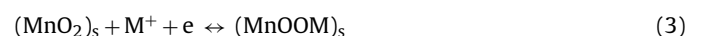
Fig. 8. Nyquist plots of MnO$_2$/polyaniline composites.

Here M = H$^+$, Li$^+$, Na$^+$ or K$^+$. The products in this study are confirmed to be amorphous nature, revealing the storage mechanism mainly comes from Eq. (3). Still, the lamellar structure (∼7 Å) of birnessite can also accommodate hydrated Na$^+$ (3.58 Å) to yield capacitance based on Eq. (4). At lower current density, the electrolyte ions can be diffused sufficiently into the interior electrode, resulting in more available surface for effective utilization of MnO$_2$ and thus a higher specific capacitance. The reduced capacitance at larger current density can be resulted from the limited diffusion time into the interior surfaces. The specific capacitance values of MP-I and MP-C composites electrodes at 1.5 mA cm^{-1} according to Eq. (2), are calculated to be 262 F g^{-1} and 134 F g^{-1}, respectively, which are comparable to the CV results. Notably, when the current density increases by an order of magnitude (i.e. 15 mA cm^{-1}), the MP-I composite electrode still delivers a specific capacitance of 186 F g^{-1} (71% of the maximum capacitance in contrast to 51% for MP-C), revealing its better rate capability. The larger specific capacitance and better rate capability of MP-I composite electrode can be attributed to the unique textural morphology: (i) the higher specific surface area offers more electroactive sites for the surface adsorption/desorption (Eq. (3)) and subsequent insertion/extraction (Eq. (4)) of protons and alkali cations; (ii) the well-defined mesoporous microstructure allows fast diffusion of electrolyte ions into the uniform mesopores due to the reduced solid-state transport length [29]; (iii) the interlink of conducting polyaniline to MnO$_2$ provides additional conductive channels for better utilization of MnO$_2$; (iv) the hierarchical hollow macropores can be served as a "ion-buffering reservoirs" for rapid Faradic reactions at high current densities [39]. The electrochemical stability of the composites electrodes is examined by charging/discharging cycling at 9 mA cm^{-1} and the capacitance retentions are shown in Fig. 7(d). It is seen that the MP-I composite electrode has a good retention of 93% of its initial capacitance after 800 cycles, showing good cycling performance. Under the similar test, the MP-C composite electrode shows much larger decrease (15%) in the specific capacitance.

The enhanced electrochemical performance of MP-I composite electrode is further confirmed by electrochemical impedance spectrum (EIS) and the resulting Nyquist plots are shown in Fig. 8. Two distinctive parts composing of Warburg arc in the high frequency region and a straight slopping line in the middle-to-low frequency region can be observed on both spectra. The high frequency arc is related to the electrolyte ions penetrating into the porous electrode materials. And the diameter of the Warburg arc represents the interfacial charge-transfer resistance (R_{ct}),

reflecting the resistance of electrochemical reactions on the electrode and is also called Faraday resistance. The R_{ct} obtained from the x-intercept of the Warburg arc are 4.4 Ω and 11.6 Ω for MP-I and MP-C electrodes, respectively. The smaller R_{ct} suggests a faster Faradic reaction with much lower resistance. The straight line with a slope from 45° to 90° ascribes to the ion diffusive impedance of electrolyte into the electrode pores. The ideal capacitive behavior is a vertical line [29]. It can be seen that the slopping line of MP-I electrode is steeper than that of MP-C, indicating a better electrochemical capacitive behavior.

4. Conclusions

Mesoporous MnO$_2$/PANi composite with unique morphology of hierarchical hollow submicron spheres was synthesized successfully by interfacial synthesis. The facile technique enables MP-I composite to show larger specific surface area (124 m^2 g^{-1}) and more uniform pore-size distribution than the composite prepared by chemical co-precipitation. The MP-I composite electrode exhibits a higher specific capacitance of 262 F g^{-1} (about twice amount of MP-C) with better rate capability and stable cyclability. The enhanced electrochemical properties of the MP-I composite electrode can be rationalized to its unique hollow microstructure with well-defined mesoporosity and the coexistence of conducting polyaniline. The results demonstrate that the development of novel MnO$_2$/conducting polymers composite holds great potential applications in high-performance electrochemical capacitors.

Acknowledgments

References

[1] P. Simon, Y. Gogotsi, Nat. Mater. 7 (2008) 845–854.
[2] B.E. Conway, Electrochemical Supercapacitors: Science Fundamentals and Technological Application, Kluwer Academic/Plenum Publisher, New York, 1999.
[3] Y. Zhang, H. Feng, X. Wang, A. Zhang, T. Xia, H. Dong, X. Li, L. Zhang, Int. J. Hydrogen Energy 34 (2009) 4889–4899.

[4] W. Wei, X. Cui, W. Chen, D.G. Ivey, Chem. Soc. Rev. 40 (2011) 1697–1721.
[5] J.G. Wang, Y. Yang, Z.H. Huang, F.Y. Kang, Electrochim. Acta 56 (2011) 9240–9247.
[6] M. Toupin, T. Brousse, D. Belanger, Chem. Mater. 16 (2004) 3184–3190.
[7] M. Toupin, T. Brousse, D. Belanger, Chem. Mater. 14 (2002) 3946–3952.
[8] S.W. Lee, J. Kim, S. Chen, P.T. Hammond, S.H. Yang, ACS Nano 4 (2010) 3889–3896.
[9] H. Zhang, G. Cao, Z. Wang, Y. Yang, Z. Shi, Z. Gu, Nano Lett. 8 (2008) 2664–2668.
[10] R. Amade, E. Jover, B. Caglar, T. Mutlu, E. Bertran, J. Power Sources 196 (2011) 5779–5783.
[11] J. Yan, Z. Fan, T. Wei, J. Cheng, B. Shao, K. Wang, L. Song, M. Zhang, F. Wei, J. Power Sources 194 (2009) 1202–1207.
[12] L. Gong, L. Su, H. Jiang, Mater. Lett. 65 (2011) 1588–1590.
[13] Z.S. Wu, W. Ren, D.W. Wang, F. Li, B. Liu, H.M. Cheng, ACS Nano 4 (2010) 5835–5842.
[14] Q. Cheng, J. Tang, J. Ma, H. Zhang, N. Shiya, L.C. Qin, Carbon 49 (2011) 2917–2925.
[15] S. Chen, J. Zhu, X. Wu, Q. Han, X. Wang, ACS Nano 4 (2010) 2821–2829.
[16] R. Liu, S.B. Lee, J. Am. Chem. Soc. 130 (2008) 2942–2943.
[17] R. Liu, J. Duay, S.B. Lee, ACS Nano 4 (2010) 4299–4307.
[18] R.K. Sharma, L. Zhai, Electrochim. Acta 54 (2009) 7148–7155.
[19] Y. Hou, Y. Cheng, T. Hobson, J. Liu, Nano Lett. 10 (2010) 2727–2733.
[20] Q. Lu, Y. Zhou, J. Power Sources 196 (2011) 4088–4094.
[21] E.C. Rios, A.V. Rosario, R.M.Q. Mello, L. Micaroni, J. Power Sources 163 (2007) 1137–1142.
[22] W. Ni, D. Wang, Z. Huang, J. Zhao, G. Cui, Mater. Chem. Phys. 134 (2010) 1151–1154.
[23] Q. Li, J. Liu, J. Zou, A. Chunder, Y. Chen, L. Zhai, J. Power Sources 196 (2011) 565–572.
[24] K.R. Prasad, N. Miura, Electrochem. Solid-State Lett. 7 (2004) A425–A428.
[25] W. Zou, W. Wang, B. He, M. Sun, Y. Yin, J. Power Sources 195 (2010) 7489–7493.
[26] J. Li, L. Cui, X. Zhang, Appl. Surf. Sci. 256 (2010) 4339–4343.
[27] R.K. Sharma, A.C. Rastogi, S.B. Desu, Electrochim. Acta 53 (2008) 7690–7695.
[28] S.R. Sivakkumar, J.M. Ko, D.Y. Kim, B.C. Kim, G.G. Wallace, Electrochim. Acta 52 (2007) 7377–7385.
[29] J.Y. Luo, Y.Y. Xia, J. Electrochem. Soc. 154 (2007) A987–A992.
[30] Y.G. Wang, W. Wu, L. Cheng, P. He, C.X. Wang, Y.Y. Xia, Adv. Mater. 20 (2008) 2166–2170.
[31] A.H. Gemeay, I.A. Mansour, R.G. El-Sharkawy, A.B. Zaki, Eur. Polym. J. 41 (2005) 2575–2583.
[32] A.H. Gemeay, R.G. El-Sharkawy, I.A. Mansour, A.B. Zaki, J. Colloid Interface Sci. 308 (2007) 385–394.
[33] Y. Furukawa, F. Ueda, Y. Hyodo, I. Harada, T. Nakajima, T. Kawagoe, Macromolecules 21 (1988) 1297–1305.
[34] Y. Li, J. Gong, G. He, Y. Deng, Synth. Met. 161 (2011) 56–61.
[35] S. Yu, J. Chen, D. Zhu, Acta Mater. Comp. Sin. 21 (2004) 1–7.
[36] N. Nuraje, K. Su, N.I. Yang, H. Matsui, ACS Nano 2 (2008) 502–506.
[37] L. Pan, L. Pu, Y. Shi, S. Song, Z. Xu, R. Zhang, Y. Zheng, Adv. Mater. 17 (2007) 461–464.
[38] S. Lowell, J.E. Shields, M.A. Thomas, M. Thommes, Characterization of Porous Solids and Powders: Surface Area, Pore Size and Density, Springer Publisher, Netherlands, 2006, pp. 43–44.
[39] C. Yuan, L. Hou, L. Yang, D. Li, L. Shen, F. Zhang, X. Zhang, J. Chem. 21 (2011) 16035–16041.